Pure Appl. Geophys. 176 (2019), 5463–5486

https://doi.org/10.1007/s00024-019-02292-3

Pure and Applied Geophysics

Spectral Wave Characteristics over the Head Bay of Bengal: A Modeling Study

Anindita Patra,[1] Prasad K. Bhaskaran,[1] and Rajib Maity[2]

Abstract—Information on spectral wave characteristics is an essential prerequisite for ocean engineering-related activities and also to understand the complex wave environment at any given location. To the best of our knowledge, there are no comprehensive studies attempted so far to study the wave spectral characteristics over the head Bay of Bengal, a low-lying deltaic environment. The present study is an attempt to describe the spectral characteristics of wave evolution across different locations over this deltaic region based on numerical simulations. Therefore, it implements a multi-scale nested modeling approach using two state-of-art wave models, WAM and SWAN, and forced with ERA-Interim winds spanning the year of 2016. Model-computed integrated wave parameters are validated against wave rider buoy data as well as remotely sensed SARAL/AltiKa and merged altimeter data. Analysis of the monthly averaged one-dimensional spectrum reveals a single peak during the southwest monsoon and existence of double peaks from November to January, and occasionally up to March. Variance energy density undergoes inter-seasonal variation and attains its maxima during the month of July. Transformation of swell wave energy as a function of depth is found to be mostly associated with physical processes such as wave-bottom interaction and attenuation by opposing winds during the northeast (NE) monsoon. Fetch restriction for the evolution of wind seas (from the NE), modification in wind shear stress by opposing swells, and bottom effects remarkably contribute to the reduction in wind sea energy at shallow water depths. This study indicates that the influence of swells is higher along the eastern side of the basin as compared to the western side, and marginally higher variance is also observed over the east except during February–April. The two-dimensional wave spectra exhibit differential wave systems approaching from various directions attributed to a reflected swell system from the south-southeast throughout the year, southwest swells, reversing wind seas following local winds, and reflected wind seas from the land boundary.

Key words: Head Bay of Bengal, SWAN, WAM, wave spectrum, wave transformation.

1. Introduction

Detailed knowledge on ocean wave characteristics is of paramount importance for the development of the marine environment, ocean engineering applications, and sustainable coastal zone management. The wave spectrum is a standard descriptor of wave characteristics as it contains information on the distribution of wave variance over both frequency and direction domains. The commonly used integrated parameters such as significant wave height (SWH) and mean wave period (MWP) provide limited information on the simultaneous occurrence of different wave systems. Engineering design and planning calculations that involve complex sea states are based on accurate wave spectral descriptions. In the spectral approach, the sea surface is represented as the superposition of a finite number of harmonic components with different frequencies and directions. The spectral components originating from different physical mechanisms play an important role in the resultant wave energy balance. The high-frequency part of the wave spectrum that is the wind-sea regime governs the exchange of momentum across the air–sea interface (Cavaleri et al. 2012). On the other hand, a proper understanding of long-period waves and their evolution is an essential prerequisite to address problems related to navigation and offshore operations, and also important in context to large-scale motions on the mooring systems (McComb et al. 2009). The concurrent existence of locally generated wind seas and remotely forced swells can lead to complex wave systems that are quite common in the global oceans. By analyzing the wave spectrum, the different wave systems present at a given location can be identified (Soares 1991; Hanson and Phillips 2001). Identification of separate wave

Electronic supplementary material The online version of this article (https://doi.org/10.1007/s00024-019-02292-3) contains supplementary material, which is available to authorized users.

[1] Department of Ocean Engineering and Naval Architecture, Indian Institute of Technology Kharagpur, Kharagpur 721 302, India. E-mail: prasadlsu@yahoo.com; pkbhaskaran@naval.iitkgp.ernet.in

[2] Department of Civil Engineering, Indian Institute of Technology Kharagpur, Kharagpur 721 302, India.

systems provides a better scope to understand the specific physical processes that determine the sea state. For a specific location, the spectral footprint is unique and depends on the prevailing meteorological and environmental conditions.

In context of the Indian seas, the Bay of Bengal and Arabian Sea experience coexistence of wind seas and swells (Baba et al. 1989; Kumar et al. 2003, 2014; Aboobacker et al. 2011a, b; Sabique et al. 2012; Nayak et al. 2013; Sandhya et al. 2016). The wave characterizations therefore need to be based on the wave spectrum rather than integral parameters in order to understand the evolution of wave energy balance. Unfortunately, there exists no detailed study on the spectral wave characteristics for the head Bay of Bengal (north of 20°N) region. The study region (Fig. 1) located in the North Indian Ocean is a quite unique region in the world owing to high tidal range, low-lying topographic features, a large riverine delta system, excessive sediment loads, numerous tidal creeks, and the mangrove ecosystems. As stated above, in order to have a better understanding on the effect of waves over this highly dynamic nearshore region, it is necessary to investigate each spectral component separately. The Bay of Bengal is exposed to a wind system of high seasonal variability, with strong winds from the southwest direction during the southwest monsoon period (June–September), from the northeast during the northeast (NE) monsoon period (November–January), and fair weather during the rest of the months. Due to the reversing wind system, one can expect intra-annual variability in the locally generated wind seas. On the other hand, swells generated from the Southern Ocean are known to travel over long distances with minimum attenuation and simultaneously interact with the locally generated wind waves over the Bay of Bengal basin. The nature of Southern Ocean swells also varies over a year with maximum energy during the Southern Hemisphere winter (June–September) followed by the spring. Therefore, a detailed analysis covering a period of one full year can provide vital information on the evolution of wave spectral characteristics.

Numerical models constitute the basis to characterize the wave conditions when measurements are not available. The state-of-art third-generation wave models have gained popularity on the account of their sophisticated physics and advanced numerics and have been successfully applied to various regions in the world by many researchers (Wang and Swail 2002; Shanas et al. 2017; Akpinar et al. 2012, 2016). With recent developments in computational power,

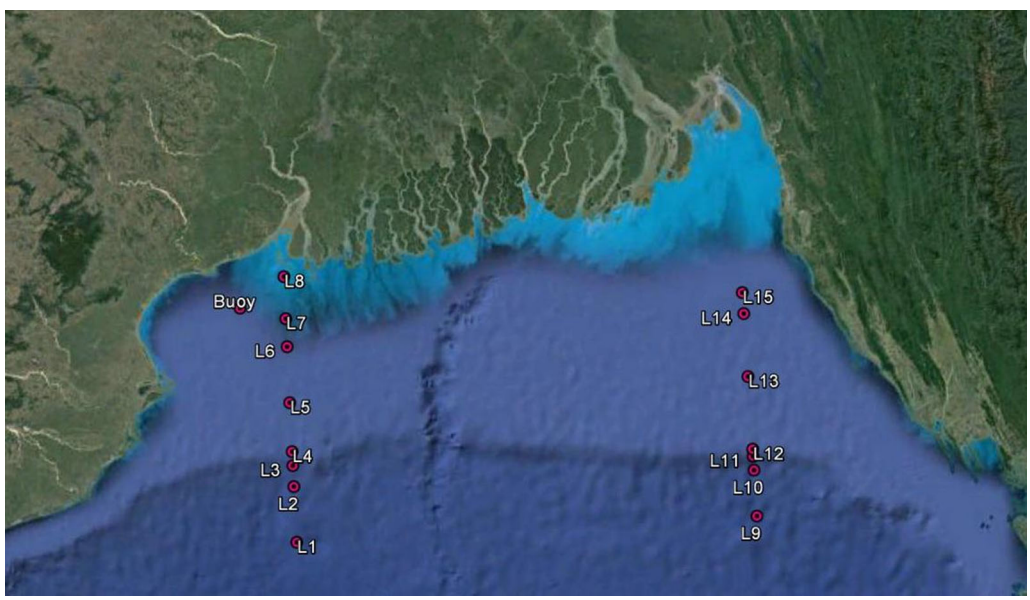

Figure 1
Study region along with locations considered for analysis

the present generation state-of-art models have the ability to model nearshore regions and complex coastline geometry with high spatial resolutions. Wave modeling using the Simulating Waves Nearshore (SWAN) model was carried out for different geographical regions such as the Chabahar zone (Saket et al. 2013), the Persian Gulf (Moeini et al. 2012), Iranian seas (Mazaheri et al. 2013), and the Black Sea (Akpinar et al. 2012, 2016). Akpinar et al. (2012) reported on the implementation of the SWAN model forced by the ECMWF ERA-Interim data set of reanalyzed 10-m winds over the Black Sea and its validation with buoy measurements. Stopa et al. (2011) investigated wave energy resources for the Hawaiian Islands in the mid-Pacific using WAVEWATCH-III and SWAN. The wave climate variability over the southwest western Australian shelf and nearshore region and its dependency on large-scale climate variability was studied using SWAN by Wandres et al. (2017). Nayak et al. (2013), Umesh et al. (2017), and Parvathy et al. (2017) have considered the SWAN model nested with the Wave Ocean Model (WAM, WAMDIG 1988) for nearshore wave simulation over different regions in the Bay of Bengal. Similarly, Sandhya et al. (2014) integrated two wave models, WAVEWATCH-III (Tolman 1991) and SWAN (Booji et al. 1999), to study the wave characteristics at coastal Puducherry on the east coast of India. Therefore, wave information derived from numerical models is of great importance to the scientific and engineering community.

There are studies (Patra and Bhaskaran 2016, 2017) that described the wave climate based on integral wave parameters, such as significant wave height (SWH) and mean wave period (MWP) over the head Bay of Bengal region. However, when two or more wave systems are simultaneously present, the integral parameters become insufficient to fully represent the wave climate. Under this condition, the spectral details are essential for many applications like climate assessment, navigation, coastal engineering, etc. The purpose of the present study is to explore the wave spectral features over this region. To accomplish this, two wave models, viz. WAM and SWAN, were nested such that the time-varying boundary spectral information from WAM was provided to SWAN, and the resultant wave spectrum obtained from fine-resolution SWAN was used for further analysis. Accordingly, the model simulation was carried out for the full year of 2016 in order to examine the seasonal and intra-annual variability. As the availability of in situ measured buoy data was limited for a short period, the model-computed SWH values have been verified accordingly. The wave rider buoy data was obtained from the Earth System Science Organization (ESSO)—Indian National Centre for Ocean Information Services (INCOIS). Further, the study also verified the model generated SWH with the satellite passes of SARAL/AltiKa over this region. Investigation on the wave evolution characteristics used the location-specific 1D and 2D spectrum derived from the model. A detailed investigation was carried out to examine the monthly variation in variance density, as well identification of separate wave systems in the study region. Diurnal variability and transformation of wave spectra along various water depths are discussed. In addition, wave spectra along two longitudinal transects over the eastern and western side of the study domain are also compared. This paper is organized as follows: Sect. 2 describes the study area and data sets used; Sect. 3 provides information on the model configuration and validation exercise, Sect. 4 provides details on the results and discussion; and, finally, the Sect. 5 discusses the overall summary and conclusion.

2. Study Area and Data Sets

2.1. Study Area

The study area as shown in Fig. 1 is bounded between the geographical coordinates 86–93°E and 19.5–23°N and situated at the northward limit of the Bay of Bengal. The study region is bounded by the West Bengal coast along the west and the Bangladesh coast on the east. This area is characterized by reversing monsoon winds and is also highly prone to tropical cyclones. The highest tidal range on the east coast of India exists over this region. Moreover, the head Bay of Bengal region is encompassed by numerous riverine networks such as the Ganges, Brahmaputra and Meghna (GBM) which is known to be the highest contributor of sediment load discharge

in the world. Also, the highly dynamic GBM delta houses the world's largest mangrove forest, the Sundarbans. In a geomorphic sense, the geometry of this region as a first approximation is a funnel-shaped bay with a wide continental shelf, numerous river drainage systems, and shallow bathymetry protected by mangrove forests.

2.2. Wind Data

Wave models are extremely sensitive to the quality of input wind forcing, and demand high-resolution and quality wind data in order to simulate realistic wave conditions. This study used the wind data (U and V components) at 10-m height obtained from the ERA-Interim data set. The ERA-Interim data set is the most recent global reanalysis data product produced at the European Centre for Medium-Range Weather Forecasts (ECMWF). The quality of the ERA-Interim product is better and accounts for the recent satellite altimeter data merged with the built-in ERA-40 data assimilation. Dee et al. (2011) provides more insight and details on the ERA-Interim product. This wind data set used in the present study is well calibrated (Stopa and Cheung 2014) and also widely used for modeling purposes (Akpinar et al. 2012; Samiksha et al. 2015; Shanas et al. 2017). The wind fields (U and V components) are available at every 6-h interval at multiple grid resolutions dating from 1979 (http://apps.ecmwf.int/datasets/data/interim-full-daily/levtype=sfc/). The present study used six hourly wind fields for the full year of 2016.

2.3. Wave Data

The present study used the measured wave data recorded by a moored Datawell directional waverider (DWR-MkIII) buoy (Barstow and Kollstad 1991) located off the Digha coast (87.65°E, 21.29°N) in West Bengal at a water depth of $\sim$ 15 m (shown in Fig. 1). This directional wave-rider buoy measures the heave motion within -20 to $+20$ m of surface elevation with an accuracy of 3%, and wave period ranging between 1.6 and 30.0 s. The wave direction measurement using the DWR-MkIII covers the range between 0° and 360° with a directional resolution of 1.5° and accuracy of 0.5° with respect to magnetic north. The data sampling duration is about 17 min for every 30 min at a frequency of 1.28 Hz. A low-pass filter with a cutoff frequency of 0.58 Hz is applied to all outputs of the buoy sensors as high-frequency measurements are prone to noise. Buoy-measured SWH data was obtained from the Indian National Centre for Ocean Information Services (INCOIS) during the period from 21 January to 20 July, 2016.

2.4. Altimeter Data

The present study also used SWH data from altimetry observations of multi-satellite missions in order to validate the model-computed wave heights. The merged satellite altimeter data are available for download from the French Research Institute for Exploitation of the Sea/Laboratory of Oceanography Space website and available from the following URL link: ftp://ftp.ifremer.fr/ifremer/cersat/products/swath/altimeters/waves/documentation/publications/. The raw data was pre-processed using the Basic Radar Altimetry Toolbox (BRAT) version 3.1.0 (Rosmorduc et al. 2011). More details on the data processing procedures are available in Patra and Bhaskaran (2016, 2017). Final post-processed data obtained from the daily records of SWH are then monthly averaged at a spatial resolution of $0.1° \times 0.1°$ for further analysis.

2.5. SAtellite for ARgos and ALtiKa (SARAL/AltiKa)

The SARAL/AltiKa, a joint mission under the Indian Space Research Organization (ISRO) and Centre National d'Etudes Spatiales (CNES), France, uses a Ka-band (35.75 GHz) altimeter system unlike other altimeters with Ku-band frequencies. The AltiKa of the SARAL mission has an objective to provide altimetry measurements to study sea surface elevation and ocean circulation characteristics preserving the similar accuracy provided by ENVISAT and JASON missions. The Ka-band altimeter used is the first oceanographic altimeter that operates using a high frequency. It is important to note that the Ka band can provide more accurate measurements in both spatial and vertical resolutions that enable better observation of coastal areas, inland water bodies, and

ice cover. The use of high frequency minimizes the ionospheric perturbations. It has a repeat cycle of 35 days and provides SWH, sea level anomaly, and wind speed. The data sets are available from ISRO (http://www.mosdac.gov.in), AVISO (http://www.aviso.altimetry.fr), and the TUDelft RADS database (http://www.rads.tudelft.nl/rads/rads.shtml). In this study, the SWH observations along the track of SARAL/AltiKa were used to validate the model-computed wave height. The track data are considered within a 10-km spatial window for collocation. Thereafter, the SWHs at these collocation points for a particular location of interest are averaged.

3. Methodology

3.1. Model Setup

Numerical wave models are tools that can be used to study the space and time evolution of surface gravity waves over a given region of interest. This study used a numerical wave model suitably configured for the head Bay of Bengal region using a multi-scale nested domain (shown in Fig. 2). The advantage in using a multi-scale nested approach is to reduce computational time as well leverage the employability of a high-resolution grid for the region of interest. In this context, the third-generation wave model WAM-Cycle 4.5.3 was used to simulate waves over the outer domain (marked as D1 in Fig. 2) that extends up to 70°S in order to facilitate the free propagation of Southern Ocean swells into distant regions and that can influence by modifying and modulating the local wind waves elsewhere. In a study by Nayak et al. (2013), the influence of long swells travelling from the Southern Ocean, crossing the hemisphere and influencing the local wind-wave regime off Kalpakkam coast in Tamil Nadu coast was reported. The readers can refer to Gunther and Behrens (2011) for more details on the WAM 4.5.3 model. As seen from Fig. 2, the intermediate domain (D2) uses the time-varying spectral boundary information generated by the coarse grid WAM model run, and, subsequently, the boundary information for the D3 domain is provided by the SWAN model run of the D2 domain. The region of interest is the D3 domain that covers the head Bay of Bengal, and the SWAN model's computed parameters are analyzed over this region. The SWAN model was customized for both the intermediate (D2) and inner (D3) domains because of its better performance in handling wave transformation processes for coastal and nearshore locations. More details on the physics and numerical formulations are available in Holthuijsen et al. (1993), Ris et al. (1999), Booij et al. (1999) and Zijlema and van der Westhuysen (2005).

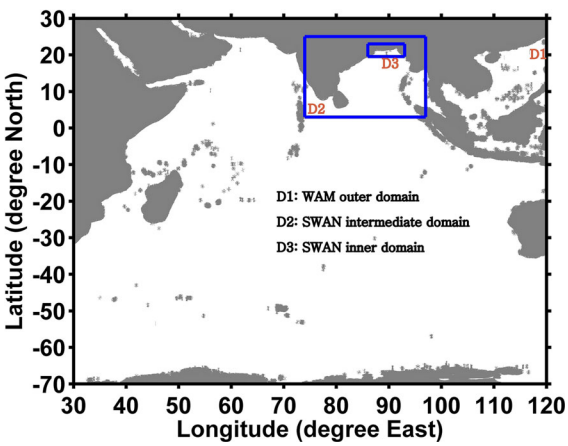

Figure 2
Multi-scale domains used for wave modeling

The SWAN model was executed in a non-stationary mode forced with time-varying wind fields and bathymetry, and, as mentioned, the model outputs are sensitive to the quality of the input data. In this study, the bathymetric data was extracted from the global ETOPO1 database of a $1' \times 1'$ grid resolution for the entire region that covers both the North and South Indian Ocean (30°N–70°S, 30–120°E). The ERA-Interim winds at 6-hour intervals were used to force the wave model that simulated waves for all the three domains having different spatial resolutions (Table 1). Finite difference grids were used to compute the wave parameters across all the domains. Frequency-direction space for SWAN was discretized using 36 directional bins and 28 frequency bins ranging between 0.04 Hz and 0.5 Hz, sufficient to represent well the overall wave energy distribution for different spectral components. The SWAN wave model run was executed in a two-dimensional non-stationary mode using the spherical coordinate system. The model physics are based on

Table 1

Study region along with locations considered for analysis

Domain	Spatial extent	Model used	Computational grid	Input wind	Time step (min)	Frequency	Directional resolution
D1	30°E–120°E, 30°N–70°S	WAM	1° × 1°	ERA-Interim (1° × 1°)	20	0.04–0.41 Hz, 25 frequencies	30°
D2	74°E–97°E, 3°N–25°N	SWAN	0.25° × 0.25°	ERA-Interim (0.125° × 0.125°)	30	0.04–0.50 Hz, 28 frequencies	10°
D3	86°E–93°E, 19.5°N–23°N	SWAN	0.01° × 0.01°	ERA-Interim (0.125° × 0.125°)	30	Same as D2	10°

third-generation mode for wind input, quadruplet wave–wave interactions, and white-capping source functions (more details in the SWAN technical manual, The SWAN Team 2012). In this study, the wind input source function based on Janssen (1989, 1991) for exponential growth and Cavaleri and Malanotte-Rizzoli (1981) for linear growth was used. The depth-induced wave breaking was accounted for using the default options. Bottom friction was modeled using JONSWAP (Hasselmann et al. 1973) with a friction coefficient $C_f = 0.67$ m^2s^{-3} and the triad wave–wave interaction activated using the default value of the lumped triad approximation (LTA) method (Eldeberky 1996). The first-order upwind backward space/backward time (BSBT) numerical scheme was considered for the discretization in geographical space. This scheme is unconditionally stable, monotonic, but rather diffusive and chosen over non-monotone higher-order linear schemes which produce un-physical results in the vicinity of sharp gradients in the grid (The SWAN Team 2012). Model runs were performed from January to December 2016, and the computed parameters are saved at 6-h intervals. Spectral information of wave energy density is computed for the 16 different locations having varied water depth as shown in the map (Fig. 1), and details of these locations are shown in Table 2.

Table 2

Details of transect locations used for analysis

Locations	Longitude and latitude	Water depth (m)
L1	(88.00°E, 19.60°N)	1614
L2	(88.00°E, 20.00°N)	1069
L3	(88.00°E, 20.15°N)	558
L4	(88.00°E, 20.25°N)	192
L5	(88.00°E, 20.60°N)	98
L6	(88.00°E, 21.00°N)	48
L7	(88.00°E, 21.20°N)	25
L8	(88.00°E, 21.50°N)	13
L9	(91.50°E, 19.60°N)	1657
L10	(91.50°E, 19.93°N)	1063
L11	(91.50°E, 20.03°N)	541
L12	(91.50°E, 20.08°N)	202
L13	(91.50°E, 20.60°N)	86
L14	(91.50°E, 21.05°N)	54
L15	(91.50°E, 21.20°N)	24
Buoy location	(87.65°E, 21.29°N)	15

3.1.1 Assessment of Model Performance

The model performance was assessed based on different statistical measures that compared the simulated SWH against observed data. The correlation coefficient (CC), bias, normalized bias (NBIAS), root mean square error (RMSE), normalized standard deviation (NSTD), and scatter index (SI) are estimated as:

$$\mathrm{CC} = \frac{\sum_{i=1}^{n}(Y_{mi}-\bar{Y}_m)(Y_{oi}-\bar{Y}_o)}{\sqrt{\sum_{i=1}^{n}(Y_{mi}-\bar{Y}_m)^2}\sqrt{\sum_{i=1}^{n}(Y_{oi}-\bar{Y}_o)^2}},$$

$$\mathrm{BIAS} = \frac{1}{n}\sum_{i=1}^{n}(Y_{mi}-Y_{oi}),$$

$$\mathrm{NBIAS} = \frac{\mathrm{BIAS}}{\bar{Y}_o}\times 100,$$

$$\mathrm{RMSE} = \sqrt{\frac{1}{n}\sum_{i=1}^{n}(Y_{mi}-Y_{oi})^2},$$

$$\mathrm{NSTD} = \frac{\sqrt{\frac{1}{n}\sum_{i=1}^{n}(Y_{mi}-\bar{Y}_m)^2}}{\sqrt{\frac{1}{n}\sum_{i=1}^{n}(Y_{oi}-\bar{Y}_o)^2}},$$

$$\mathrm{SI} = \frac{1}{\bar{Y}_o}\sqrt{\frac{1}{n}\sum_{i=1}^{n}\left[(Y_{mi} - \bar{Y}_m) - (Y_{oi} - \bar{Y}_o)\right]^2},$$

where n represents the number of data pairs; Y_{mi} and Y_{oi} are the model outputs and observed values, respectively. $\bar{Y}_m$ and $\bar{Y}_o$ are the averaged values corresponding to the model and observation, respectively.

3.2. Model Validation

The directional waverider buoy off the Digha coast (shown in Fig. 1) is the only source of in situ observation available in the study region and also used for the validation of model-computed SWH for a limited duration (January–July 2016). Model-derived wave parameters were compared with the measurements at the buoy location to verify the efficacy of the reanalysis wind-driven model output. Figure 3 a provides a comparison of the time series of SWH for the period from 21 January to 20 July barring the spin-up time. As seen from this figure, the general agreement between model and measured data looks reasonable. Table 3 provides the error metrics based on statistical measures for the model-computed SWH against buoy measurement off the Digha coast. The corresponding values of bias, RMSE, and scatter index for SWH are −0.06 m, 0.24 m, and 0.21, respectively. The higher correlation coefficient (0.87) draws attention to the fact that simulated SWH closely follows the measured SWH across the entire length of the buoy record. The normalized standard deviation reveals that model SWH has lower variability as compared to the observed values. The lower variability of ERA-Interim data implies a smoother data set lacking detailed processes and weather extremes (Stopa and Cheung 2014). Error statistics of wave height indicate that the model simulations

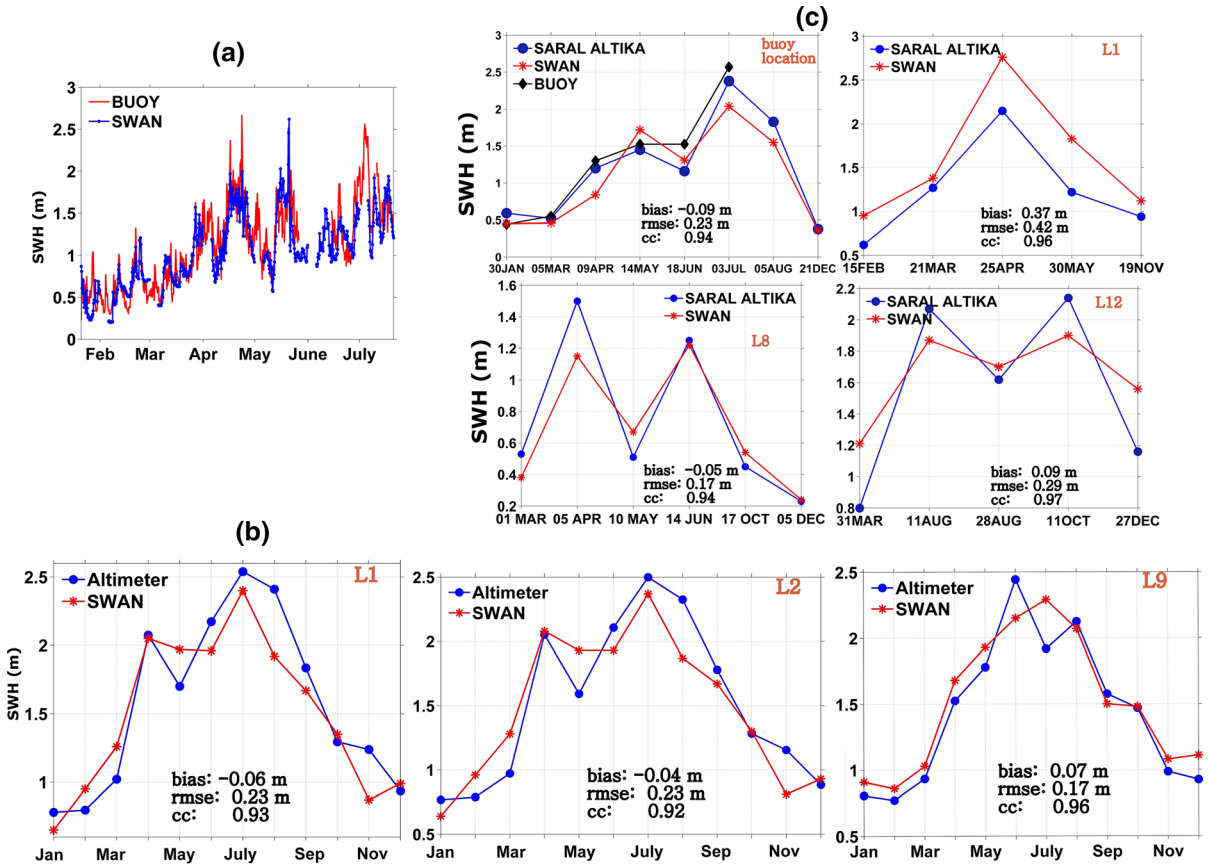

Figure 3
Comparison of significant wave height between **a** SWAN and wave rider buoy, **b** SWAN and altimeter, and **c** SWAN and SARAL/AltiKa

Table 3

Model-computed error metrics against measured buoy data off the Digha coast during the period January–July 2016

	Mean (SWAN)	Mean (buoy)	CC	Bias	NBIAS (%)	RMSE	NSTD	SI
SWH	1.04 m	1.10 m	0.87	− 0.06 m	− 5.10	0.24 m	0.93	0.21

CC correlation coefficient, *NBIAS* normalized bias, *RMSE* root mean square error, *NSTD* normalized standard deviation, *SI* scatter index

are suitable for further analysis. The discrepancy evidenced in model outputs may be due to the limitation in ERA-Interim winds and short duration of comparison. However, the wave model outputs are much better than ERA-Interim wave parameters (which are from a global WAM run) as seen from Table 2 reported by Patra and Bhaskaran (2017). In addition, the measured wave spectrum for this location is not available in the public domain. Therefore, the model-computed wave spectrum is the only source available for analyzing the spectral behavior over this region of interest.

In addition, the model-simulated SWHs are also compared with altimeter-derived SWHs from different missions for the full year of 2016. Time series comparisons of the monthly averaged values at three locations (L1, L2, and L9) are shown in Fig. 3b. The figure clearly shows that model SWHs are fully consistent with the altimeter records. The high correlation coefficient (≥ 0.92), almost no bias (≤ 7 cm), and small RMSE are noticeable for all the three selected locations. In addition to comparison with altimeter records, the present study also made an attempt to compare model-computed results with high-resolution SARAL/AltiKa data (shown in Fig. 3c). The comparison was made at four different geographical locations, viz. L1, L8, L12, and the buoy location. The locations L1 and L12 are at relatively larger water depths at/off the shelf break regions, whereas L8 and the buoy locations are in the coastal waters. Results clearly demonstrate that the model-computed wave heights match reasonably well with the high-resolution SARAL/AltiKa data. The general observation from Fig. 3c is that locations in the coastal waters (L8 and buoy location) portray a better match. The error statistics show a higher correlation coefficient and negligible bias except at L1 which is far away from the coast. The observed bias and RMSE at L1 are 0.37 m and 0.42 m, respectively. The overall observation is that SWHs from the directional wave rider buoy off the Digha coast and AltiKa and SWAN model closely follow each other. Moreover, the AltiKa is a Ka-band altimeter proven to be much superior as compared to other satellite missions, and this provides an opportunity to validate model-computed wave height at the coastal regions. The validation exercise shows significant match between model and the satellite records.

4. Results and Discussions

4.1. Monthly Variability of 1D Wave Spectra

This section analyses the 1D wave spectra obtained from model simulations. Monthly averaged 1D wave spectra at a deep water location L1 and the Digha buoy location are presented in Fig. 4. The top panels in Fig. 4a–c show the monthly energy density for location L1, and the bottom panels shown in Fig. 4d–f correspond to the buoy location. The wave spectrum at L1 consists of multiple peaks during January 2016 (Fig. 4a). The narrow-banded distinct mature swells of frequency in excess of 15 s are present along with one predominant swell peak (9.81 s) and wind-sea peak (4.64 s). The energy density corresponding to wind-sea peak is centered at 0.17 m^2/Hz, and this diminishes to almost half for the swell peak. From February to April, the variance density has magnified gradually rising to 2.46 m^2s^{-1}. The wind-sea peak frequency has shifted towards the lower lobe with increased energy. Mature swells persist, but the predominant swell system observed in January is not seen during this period except March. The monthly averaged spectrum for May is single-peaked with a peak value of 2.10 m^2/Hz at 9.81 s. This peak energy is seen reducing during May and June, although the low-frequency part magnifies as

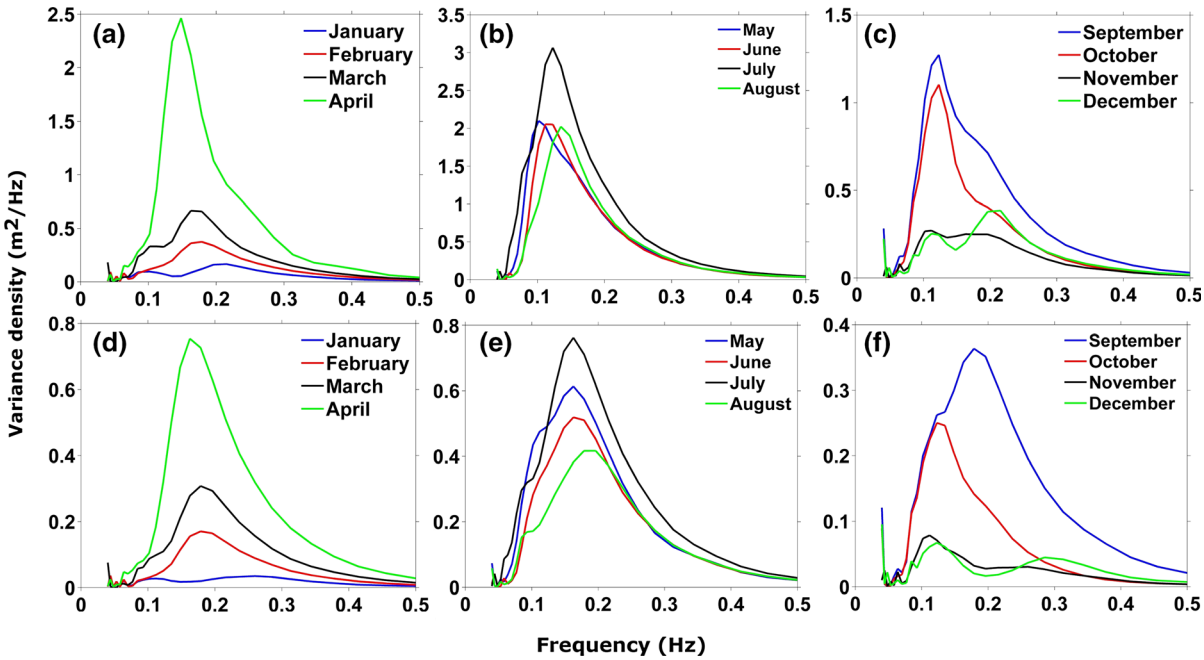

Figure 4
Monthly variation of 1D spectrum at L1 (upper panel) and at the buoy location (lower panel)

compared to April. During July, it reaches the maximum peak energy (3.06 m^2/Hz) during the year. Moreover, the variance density is almost the same in magnitude as during April at the higher-frequency part (> 0.15 Hz). The energy level during July is dominant as compared to all the months for both wind sea and swells. During August, the peak energy had reduced, and the peak frequency shifts towards the higher side. During the southwest (SW) monsoon, the spectra are single-peaked, maintaining a peak period around 8 s. Thereafter, the peak energy has declined successively until November. The wind-sea part of the spectra has decreased abruptly from September to October. Hence, October experiences single-peaked and swell-dominated waves having peak frequency around 8.14 s. Two well-separated peaks are evident during November and December. During the NE monsoon period, wind sea dominates, as compared to swells, having its utmost influence during December.

The magnitude of variance density at the buoy location is notably less as compared to L1, but the monthly variation closely follows the above. The wave spectrum at this point consists of multiple peaks during January (Fig. 4d). The peak is centered at 3.85 s for the higher-frequency side and at 8.94 s for the lower-frequency side of the spectrum. It implies the presence of both wind sea and swell components coexisting together. The maximum variance density during January is limited to 0.04 m^2/Hz. From February to April, the variance density had amplified gradually and was also noticed in the peak period of wind seas. During April, the variance density is 0.76 m^2/Hz, which is more than double the peak energy density during the previous month. The peak period is around 6–7 s from May to July, and the peak energy value during July is 0.76 m^2/Hz, the highest amongst all months. In August, the variance density reduces by almost half, and the peak frequency shifts towards the higher side. In the deep-water case (for location L1), the spectral peak is around 8 s during the SW monsoon, and it is around 6 s for the buoy location (refer to Table 4). In spite of strong winds and swell influence, a single peak is noticed at this location due to redistribution of wave energy in the spectral frequency bands. In October, the peak frequency increased to 8.14 s owing to swell dominance. It is seen that the peak corresponding to wind seas is lower during November–December as compared to a low-frequency peak, unlike the

Table 4

Peak period and energy density for the monthly averaged 1D spectrum at transect locations over the west

Months	Deep water location: L1 (1614 m)		Shallow water location: L8 (13 m)		Buoy location (15 m)	
	Peak period (in s)	Peak energy density (m^2/Hz)	Peak period (in s)	Peak energy density (m^2/Hz)	Peak period (in s)	Peak energy density (m^2/Hz)
Jan.	9.81/4.64	0.10/0.17	8.94/4.64	0.02/0.02	8.94/3.85	0.03/0.04
Feb.	5.60	0.38	5.10	0.14	5.60	0.17
Mar.	9.81/6.15	0.33/0.67	5.10	0.27	5.60	0.31
Apr.	6.75	2.46	5.60	0.64	6.15	0.76
May	9.81	2.10	8.94/6.15	0.43/0.53	6.15	0.61
June	8.94	2.05	5.60	0.37	6.15	0.53
July	8.14	3.06	5.60	0.59	6.15	0.76
Aug.	7.41	2.02	5.10	0.37	5.10	0.42
Sep.	8.14	1.27	8.14/5.10	0.23/0.27	5.60	0.36
Oct.	8.14	1.10	8.14	0.21	8.14	0.25
Nov.	8.94/5.60	0.27/0.25	8.94/3.51	0.05/0.01	8.94/3.85	0.07/0.03
Dec.	8.94/4.64	0.25/0.39	8.14/2.91	0.04/0.01	8.14/3.51	0.07/0.04

variance density spectrum at L1. The wind-sea energy is lower because of restricted fetch available for winds at the buoy location. Consequently, the wind-sea peak period is less as compared to L1. On the other hand, the swell period reduces as compared to L1 following the dispersion of water waves.

The time series analysis of wave spectra enhances the information on waves as well their physical origin which includes extreme events, any alteration in atmospheric forcing, among others. The map of wave spectral energy density as a function of frequency and time for each month is shown in Fig. 5. During June–August, it is mostly around 0.1–0.15 Hz, indicating the presence of swells. Significant wave spectral density is noticed for wave periods in excess of 10 s during this period in distinct patches. During September, the spectral energy density predominantly lies between 0.1 and 0.15 Hz and occasionally around 0.15–0.2 Hz in the low-frequency side (< 0.1 Hz). The spectra are comparatively narrow banded during the monsoon. Wave spectral density is concentrated in two separate frequency bands during November–January. One of the frequency bands lies around 0.2 Hz, due to the presence of wind waves, and the other is around 0.1 Hz, which represents the presence of swells. During February–April, the wave spectra are mainly centered between 0.12 and 0.2 Hz, indicating the dominance of wind seas. Moreover, significant wave energy is seen around 0.1 Hz during 10–13 March. During May, very high spectral energy (> 6 m^2/Hz) is seen around 20 May resulting from cyclone *Roanu* over the Bay of Bengal. On the other hand, two dominant bands (0.1–0.15 Hz and 0.15–0.2 Hz) are seen irregularly. In October, significant energy is noticed around 0.1–0.15 Hz. A depression during 2–6 November over the head Bay of Bengal enhanced the variance density around 6 November. The general observation is that wave spectral density spreads widely over frequencies for the buoy location as compared to the deep-water location (Fig. 6). The variance density corresponds to wind-sea shifts towards higher frequency and lie centered around 0.25–0.3 Hz during November, December, and January, but swells are almost in the same band. During the monsoon, the energy density concentrates mainly around 0.15–0.2 Hz and occasionally extends to the 0.1–0.15-Hz band. In October, significant energy is around 0.1–0.15 Hz with a higher directional spread about 0.15–0.25 Hz during February and March, and 0.12–0.23 Hz in April. The signature of depression is clearly seen during May and November like the case of L1.

4.2. Evolution of Wave Spectra over Varying Depths

In this section, the variation of 1D spectra at varying water depths along the two longitudinal transects is studied for each month of 2016. Figure 7 displays the spectral alteration along 88°E, the west side of the study basin. Distinct peaks corresponding

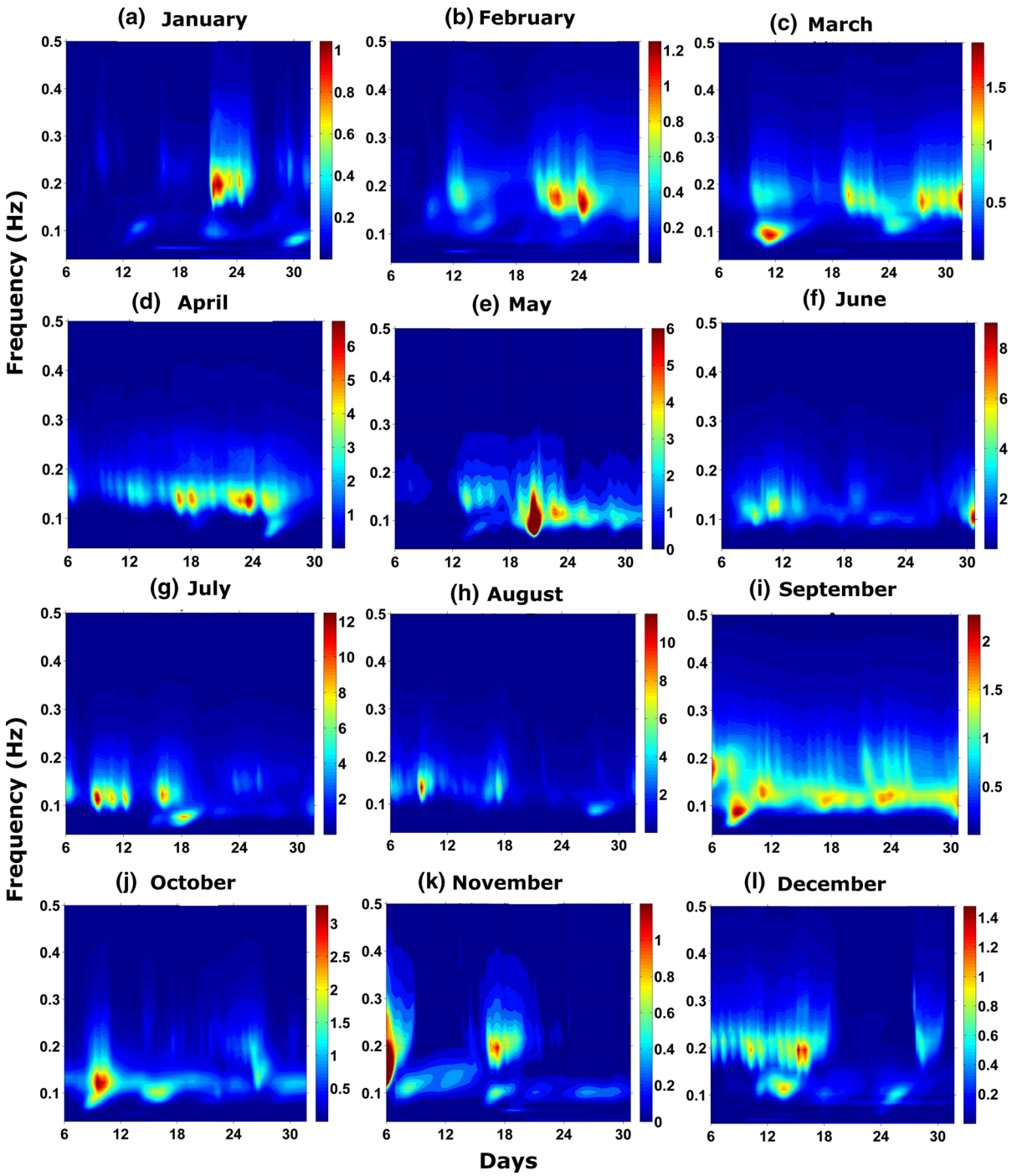

Figure 5
Time series of 1D spectra during each month at L1. The color bar indicates variance density (m^2/Hz)

to sea and swell systems are present during the NE monsoon months at varying water depths examined for the longitudinal transect at 88°E. The peak energy for the predominant swell system is almost the same from L1 to L5 (98-m depth) and decreases thereafter up to L8. This is attributable to swells propagating

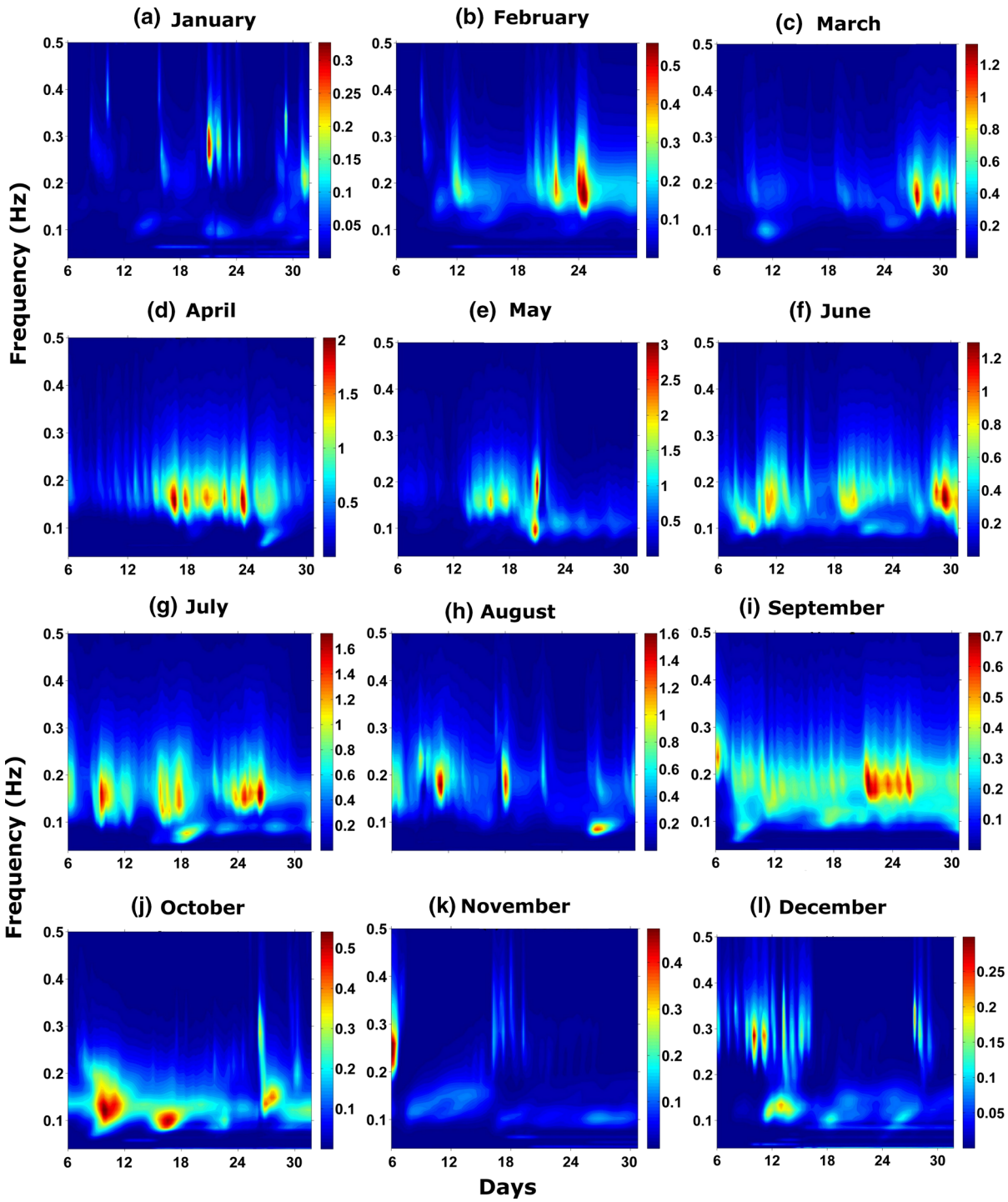

Figure 6
As Fig. 5 except at the buoy location

from deep water to the shallow water as they seldom feel the bottom up to a water depth around 100 m, and thereafter that bottom effect is notable. As Southern Ocean swells propagate opposite to winds during the NE monsoon, the attenuation of swells can be attributed to the effect of opposing wind as well as

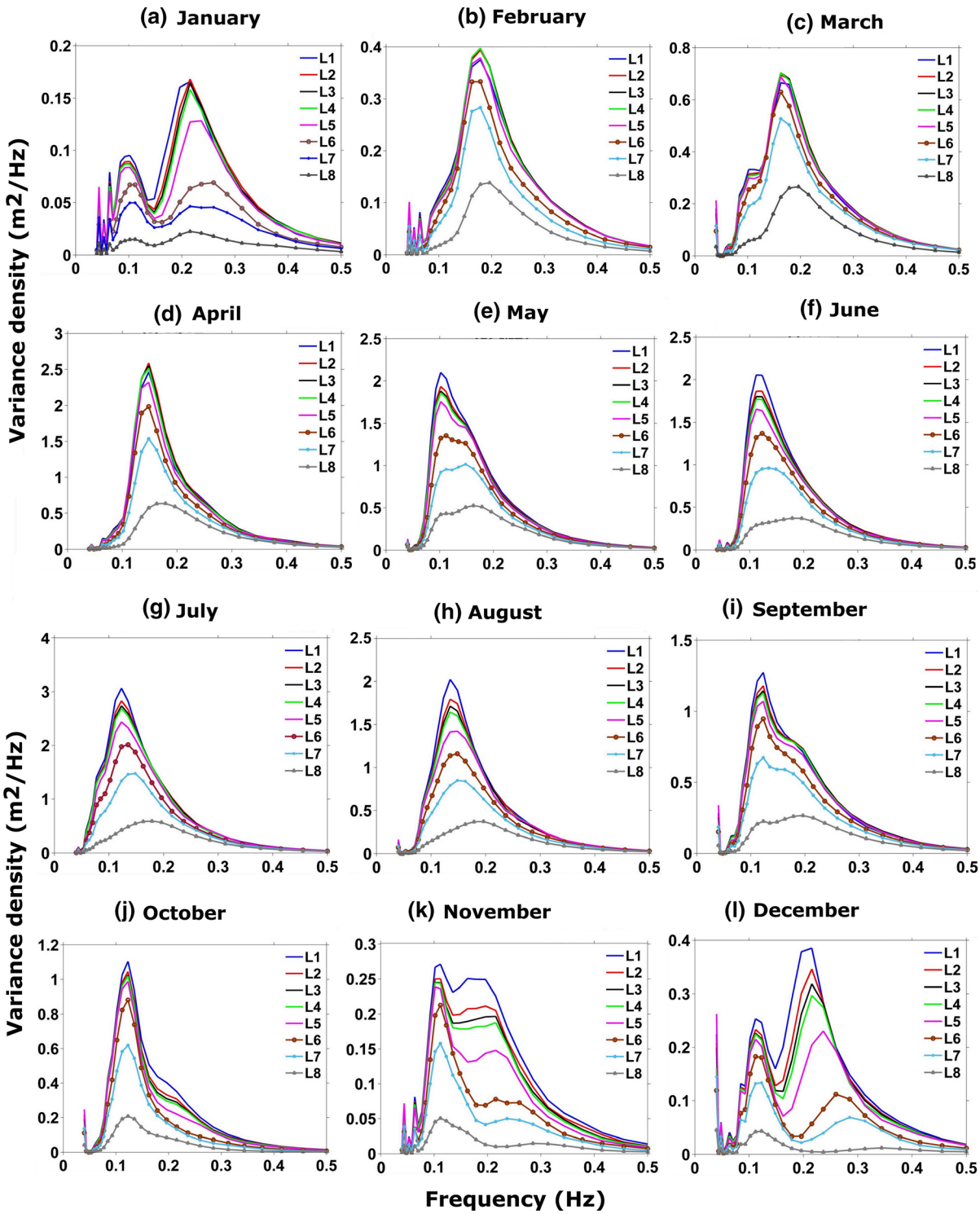

Figure 7
Comparison of monthly averaged wave spectra at different water depths along the transect at 88°E

the wave-bottom interaction. Longuet-Higgins (1969) suggests the damping of long waves in case the long waves and short waves are propagating in opposite directions, as for wind blowing against a swell. Wind seas moving away from the coast are stronger for L1–L5 as sufficient fetch is available for winds (Figure S1). This is not the case for the nearshore locations and the wind-sea peak energy is almost half at L6 than at L5. The wind-sea peak frequency increases from L5 to L6 and onwards with an exception during January from L6 to L7. During December–January, the wind-sea energy is higher than swells for deep water locations, but is lower for L6–L8. The opposing swell can intensify the NE wind sea by increasing wind shear stress towards offshore. Thus, it also contributes to the reinforcement of wind-sea energy away from the coast. During the SW monsoon, both wind seas and swells propagate from the south. Energy dissipation due to the bottom is seen clearly for the locations shallower than L5. The spectral shape becomes flattened in shallow-water locations because of deflated spectral density. The peak frequency of single-peaked spectra is seen to increase from L6 towards shore. Interestingly, double peaks are found at L8 for September and not seen at other locations. During February to April, wave energy diminishes nearshore crossing L6, and the peak period changes from L7 to L8. It is interesting to note that the peak energy is comparable between L1 and L5 and higher for L2–L4 as wind blows towards the coast (Figure S1). Accordingly, the wind seas tend to intensify towards the coast. Peak frequency remains almost constant from L1 to L8 during October because of swell dominance. This implies that peak frequency alteration with depth is mainly manifested for the wind sea part of the spectrum. The spectral evolution in May is similar to the SW monsoon months, and two separate peaks are noticed only for L7 and L8.

Another set of points along the 91.5°E (eastern side) transect have been considered to study the wave energy transformation (Fig. 8). During the NE monsoon, a drop in variance density is evident from L13 onward which is at the same latitude and almost similar water depth (86 m) as L5. Moreover, the wind-sea peak frequency shifts towards higher frequency from L13 onwards. The spectral density is slightly higher at these points as compared to locations in the same latitude along 88°E. More specifically, swells are stronger here than the locations at 88°E. This is probably associated with the direction of swell propagation as the Southern Ocean swells usually propagate from the southwest direction. In the SW monsoon, similar features as above such as the dissipation of wave energy, reduction in peak period, and flattening of wave spectra are seen from L14 onward for the considered set of points. In general, the spectral shape is narrower here as compared to the locations at the western side possibly due to more swell dominance. In addition, spectral peaks are higher over the east during the SW monsoon. The highest variance density (3.04 m^2/Hz) at L9 (Table 5) occurs during June and it is comparable with peak energy for July at L1. Comparing L15 and L7, which are at almost at similar water depths, the peak period at L15 is higher than that of L7. During May, the variation along depth is similar to the SW monsoon. The spectral peak is at higher energy than for locations on the western side. Similar features as seen along the western side are found during October. In contrast, comparably less wave energy is evident during February–April. The important thing to note here is the presence of prominent swell peaks during February and March, which is absent over the western side of the study domain. Overall, the analysis agrees with the study by Patra and Bhaskaran (2016) which showed that altimeter-derived wave height has increased more over the eastern side as compared to the western side of head Bay of Bengal. The SWAN-simulated wave spectrum for the geographic domain D2 was validated in a recent separate study by Umesh et al. (2018). The comparison between the modeled and measured wave spectra are also presented in Figs. 5 and 6 by Umesh et al. (2018). The present study used a similar model setup for nesting and wind forcing as described in Umesh et al. (2018).

4.3. Analysis of 2D Spectra

Two-dimensional wave spectra at L1 averaged over each month are shown in Fig. 9. Wave systems present at a location can be distinguished by identifying the frequency-directional behavior of the 2D

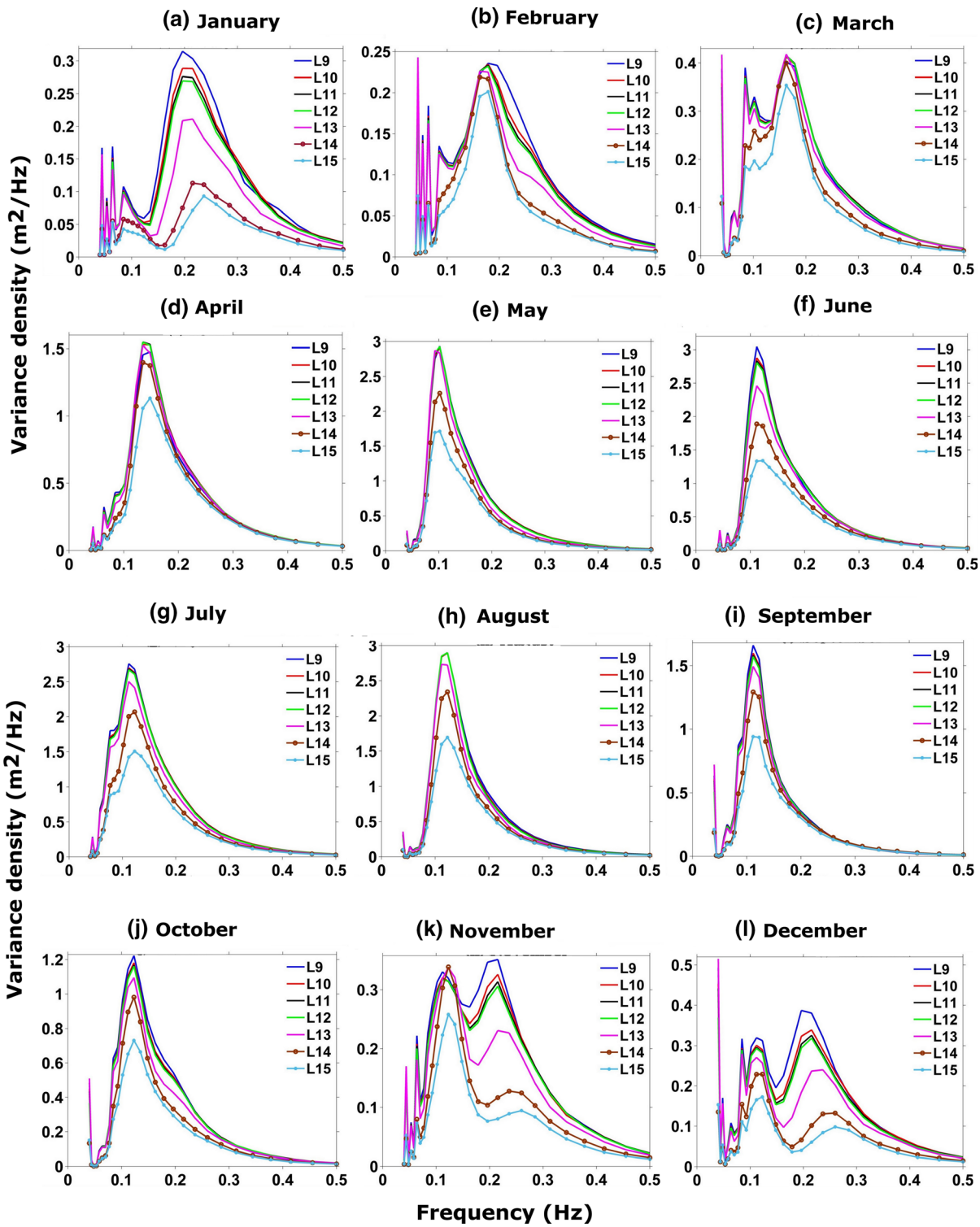

Figure 8
Comparison of monthly averaged wave spectra at different water depth along the transect at 91.5°E

Table 5

Peak period and energy density for the monthly averaged 1D spectra at transect locations over the east

Months	Deep-water location: L9 (1657 m)		Shallow-water location: L15 (24 m)	
	Peak period (in s)	Peak energy density (m^2/Hz)	Peak period (in s)	Peak energy density (m^2/Hz)
Jan	11.83/5.10	0.11/0.31	11.83/4.23	0.04/0.09
Feb.	11.83/5.60	0.14/0.24	5.60	0.20
Mar.	9.81/6.15	0.33/0.40	9.81/6.15	0.20/0.35
Apr.	6.75	1.48	6.75	1.13
May	9.81	2.93	9.81	1.71
June	8.94	3.04	8.14	1.34
July	8.94	2.76	8.14	1.51
Aug.	8.14	2.89	8.14	1.69
Sep.	8.94	1.66	8.94	0.94
Oct.	8.14	1.22	8.14	0.73
Nov.	8.94/4.64	0.33/0.35	8.14/3.85	0.26/0.09
Dec.	8.94/5.10	0.32/0.39	8.14/3.85	0.17/0.01

spectrum. Individual wave systems are energy transformation in the frequency-direction space. The wave systems can either be locally generated wind sea or a remotely generated swell system. Wind seas are defined by high frequency and larger directional spreading, whereas swells have low frequency and narrow directional spreading.

The 2D mean spectrum for January consists of both wind sea and swell components. The prominent wind seas are from the NE (northeast) direction with a frequency around 0.2 Hz and higher directional spread. In addition, another wind-sea system with lesser directional spread is also noticed from the west-southwest (WSW) direction. The low-energy wave system is observed due to waves reflected from the coastline. Low-frequency swells are evident approaching from the S (south), SSE (south-southeast), and SSW (south-southwest) directions. Distinct swell systems with a peak wave period in excess of 15 s reach from 150°. These swells are possibly reflected swells from western Australia/Indonesia. The NE monsoon is dominated by high-frequency wind seas (0.15–0.25 Hz), and from February onward, this wave system shifts to a very-high-frequency region (up to 0.35 Hz). Maximum peak spectral energy increases gradually from February onward and attains its maximal value in May. During February and March, wind seas are from the S (south) and SW (southwest) with large spreading over frequency and direction space, and swells arrive from the SE. During April and May, the wind sea shifts to lower frequency (0.08–0.25 Hz) with increased energy levels and less directional width. During June–October, energy spreading is narrow over frequency and direction space and concentrates more towards the lower-frequency side. The spectral energy propagates from the SW direction with a peak period of around 10 s. It is noteworthy that a single peak exists during the SW monsoon which is characterized by strong SW winds blowing over the region and swell dominance. The increased swell propagation from the Southern Ocean to Northern Indian Ocean basin during the months of June, July, August, and September can be attributed to the southern winter. The strong winds are capable of generating waves with low frequency and high energy. Thus, wind seas overlap with swells in the frequency-direction space. However, two distinct close peaks are seen during July when the wind reaches its maxima for that year. The energy system merges into a single peak during the rest of the SW monsoon months. Waves with the highest peak energy (0.045 m^2/Hz) are found during July. During November–December, swells are prominent, while the wind seas dominate. Though the peak energy corresponding to the swell is high, the total energy is comparatively more for wind seas by virtue of larger areal coverage. In addition to the NE direction, wind seas with low energy are seen radiating from the NW (northwest). The unidirectional swells arrive from 150° with periods in excess of 10 s almost throughout the year. Two well-separated wave systems are

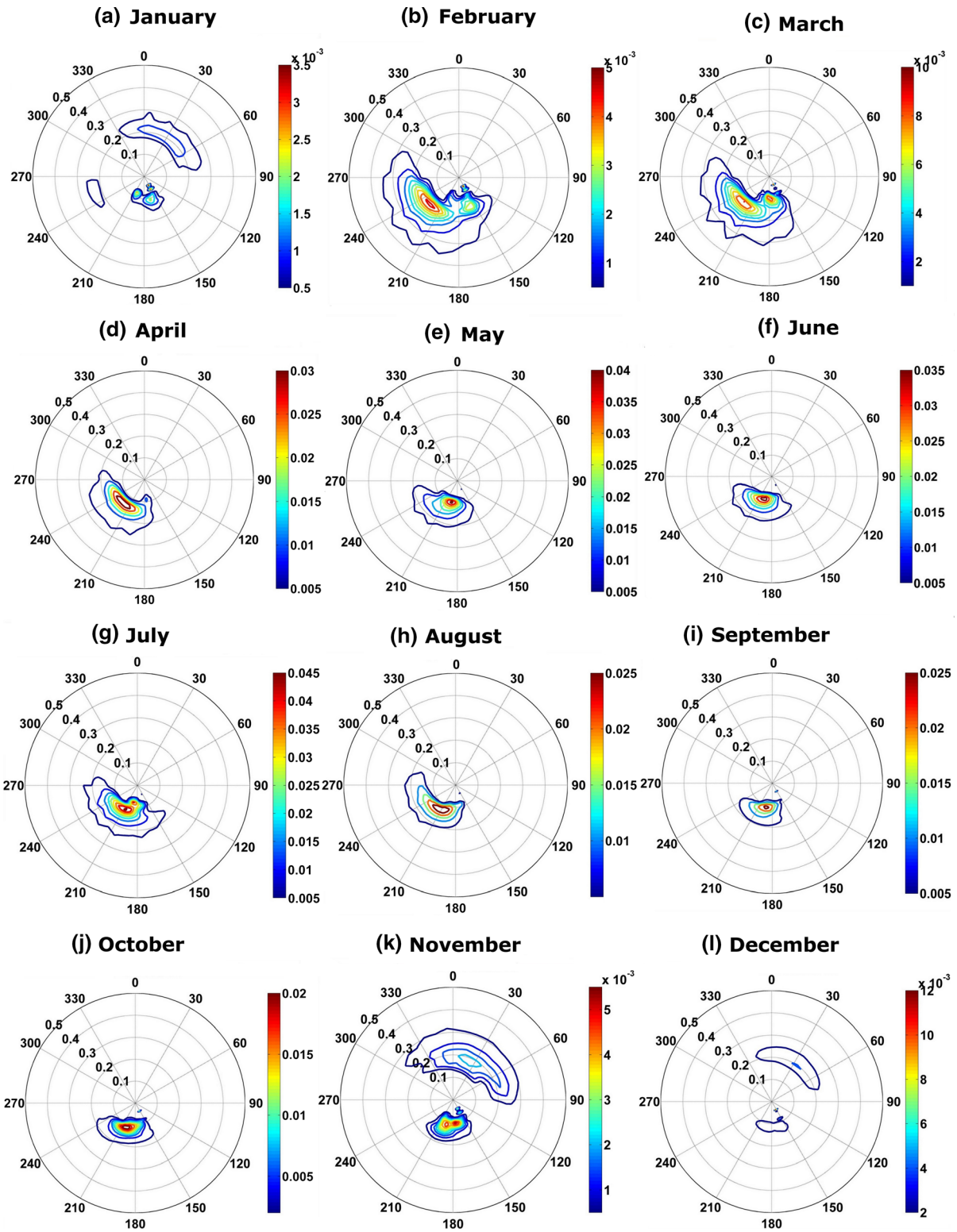

Figure 9
Two-dimensional wave spectrum at L1 during each month. The color bar indicates variance density (m^2/Hz)

detected during November to April, and that matches well with the observational evidence reported by Amrutha and Sanil Kumar (2017).

At the buoy location, the features of 2D spectra differ in frequency-direction space as compared to that of the L1 (Fig. 10) location. This is obvious due to refraction of waves, energy dissipation, and frequency shift resulting from bottom interaction. During January, the wind seas from the north are absent at the buoy location, unlike L1, because of fetch restriction. Instead, local waves arrive from the ESE (east-southeast) along with E (east) and NE directions. Another high-frequency wave system approaches the buoy location from the SSW direction with peak energy around 0.2 Hz. This particular wave system persists thereafter from February to April but with increase in energy and decrease in peak frequency. The directional width becomes narrow as compared to L1 due to confined wave propagation following the land boundary. During May, the peak period reaches almost 10 s and the peak energy is centered around 0.012 m^2/Hz. Two distinct closer peaks are visible at this point during the SW monsoon months. Waves corresponding to these peaks propagate from the SSE (swells) and SSW (wind seas) directions with comparatively high energy for wind-seas. Swell peak frequency is around 10 s and wind-sea peak frequency is centered around 6–7 s. The maximum energy observed at the buoy location is 0.012 m^2/Hz during July, and that is about four times less than L1. The month of October follows similar features like the SW monsoon months but with narrow directional width and lesser energy levels resulting from the reversal of wind systems. Though NE seasonal winds start blowing during November, waves from the NE are not noticed at this location, unlike the case seen at the L1 location. This may be due to limited fetch in the north of this point and weak winds. A narrow-banded wind-sea system advances from the NE during December. The wave spectrum contains two distinct peaks during the SW and NE monsoon at this location.

Figure 11 shows the diurnal variation of wave spectra on 8 July 2016 at the Digha buoy location. Diurnal variation includes the effect attributed due to local winds (coastal breeze). It is evident at the nearshore location, unlike the deep-water location. During early hours of the day, the spectral densities are low. The wave spectra evolve as wind speed intensifies over this region and obtain their maxima at 18 h. During July, the SW winds blows from sea to land which is higher during the afternoon hours. The peak spectral density at 18 h is almost double as compared to 00 h. The shift in peak frequency towards the lower side of the spectrum is seen to occur during late hours of the day. The peak energy level of the 1D spectrum at 06 h, 12 h, and 18 h are 0.31 m^2/Hz, 0.50 m^2/Hz, and 0.75 m^2/Hz, respectively. The peak frequency decreases from 0.20 Hz at 00 h to 0.16 Hz at 18 h. Diurnal variability during the NE monsoon is also clear from Fig. 12. It indicates the spectral energy variation during 28 December 2016. During December, coastal breeze are stronger during early hours of the day. Thus, the high-energy waves approach from a NE direction at 00 h and 06 h. The wind-sea energy is relatively lesser during the afternoon hours. Also, there is not much variability noticed in the swell wave system throughout the day. The wind-sea peak energy decreases and frequency gets lower during afternoon hours as evident from the 1D spectra. The wind-sea peak energy at 00 h is almost thrice as compared to 18 h. It is seen that the wind system plays a major role in mature wind-sea conditions during the afternoon hours. Multiple peaks associated with swells are consistent during the day.

4.4. Qualitative Case Study of Wave Spectral Characteristics

The present study is a qualitative analysis of wave spectral characteristics using a multi-scale nested modeling approach for the head Bay of Bengal region which is primarily a data-sparse region. A nested modeling system using WAM and SWAN models was adopted to understand the wave characteristics and spectral evolution of both wind seas and swells for the study region. To understand the spatio-temporal evolution of wind waves, an in-depth qualitative analysis was carried out to better understand the wave spectral evolution characteristics by carrying out model simulation for one full year. Intra-seasonal variability of wind waves in a reversing wind system for the study region has been thoroughly

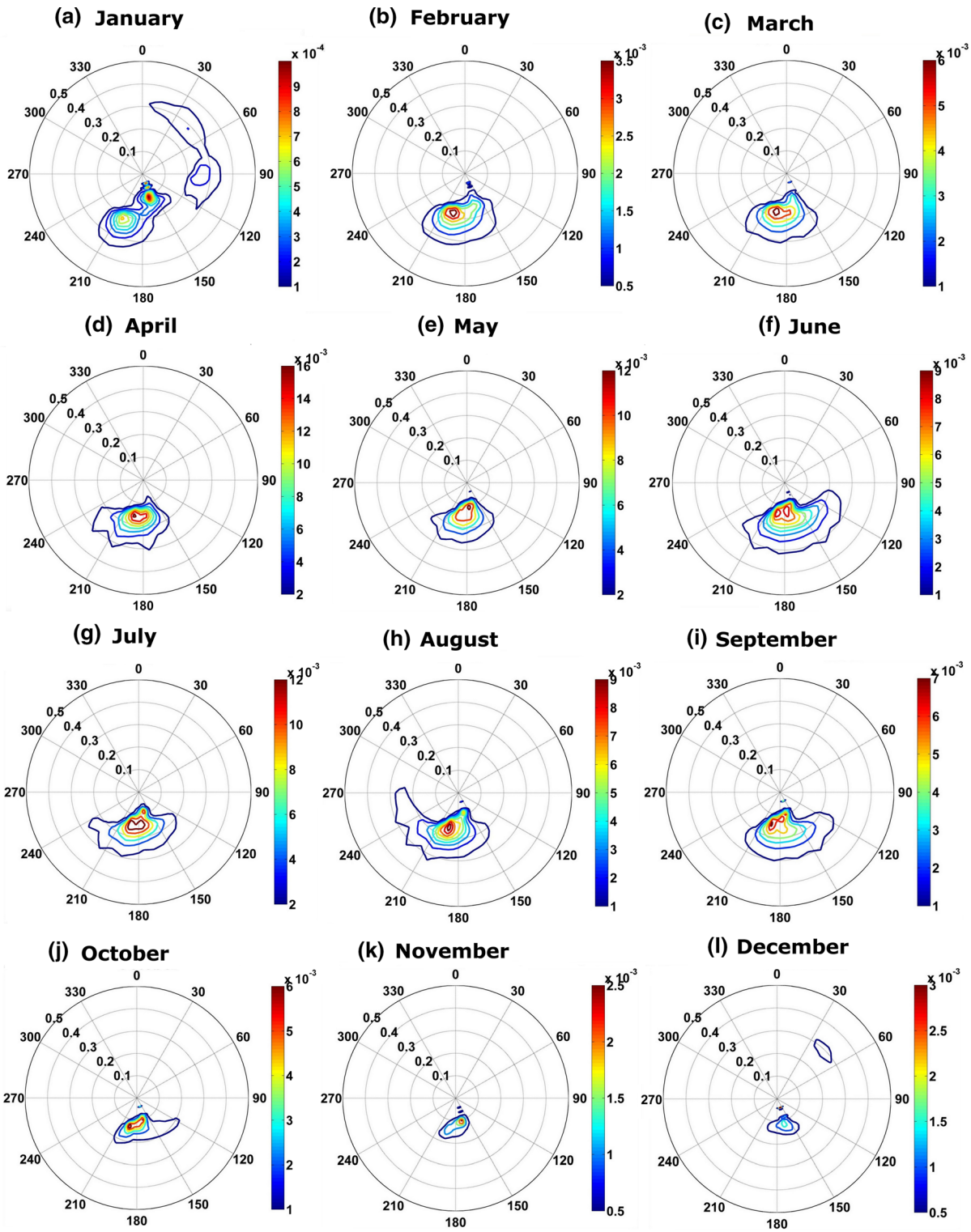

Figure 10
As Fig. 9 except at the buoy location

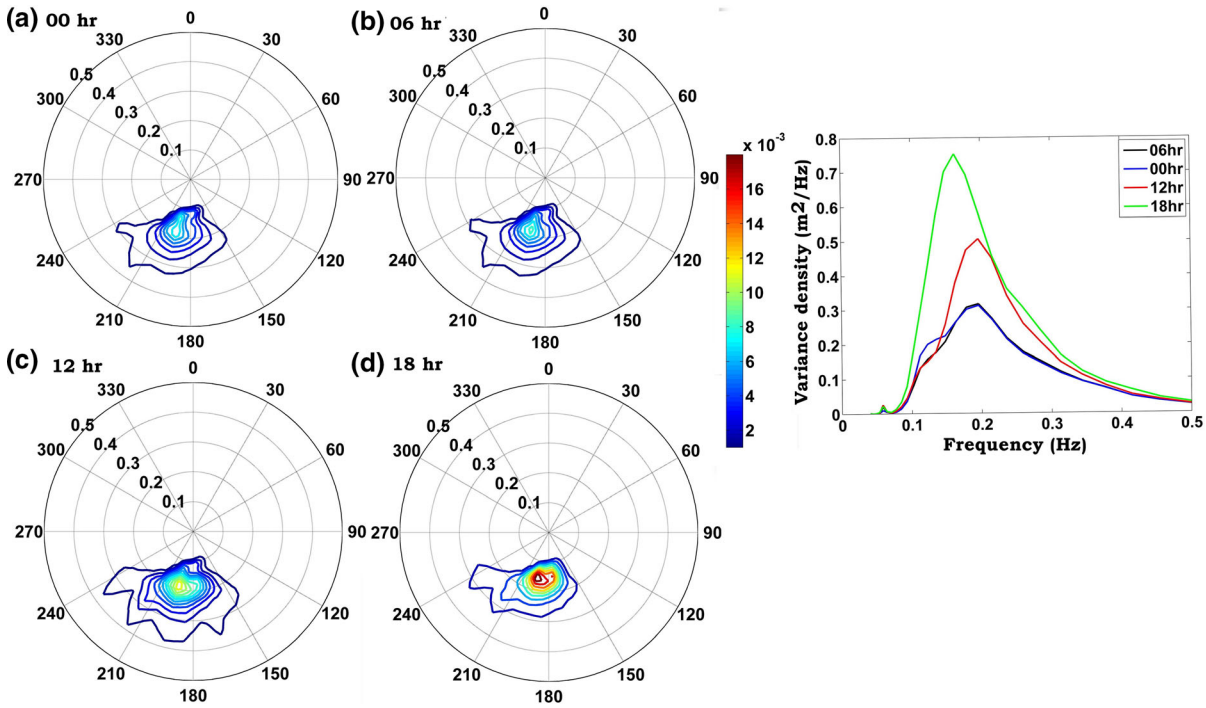

Figure 11
Diurnal variation of wave spectra during 8 July 2016. The 2D spectrum (left panel) and 1D spectrum (right panel) are presented at 6-hour intervals

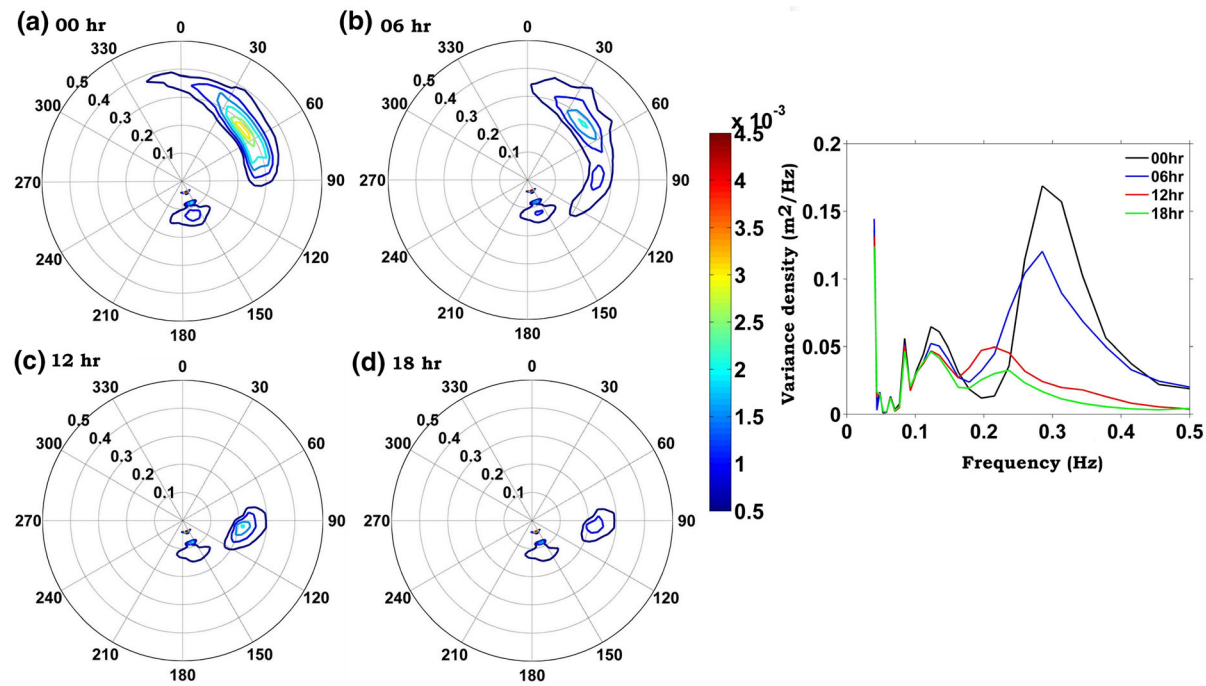

Figure 12
As Fig. 11 except during 28 December 2016

investigated. Monthly averaged wave spectra show the presence of multiple peaks, indicating the coexistence of different wave systems. This study clearly brings to light transformation of wave spectra in both wind seas and swell systems for water depths beyond 100 m towards the coast. Qualitative analysis of wave spectra indicates that during the post-monsoon season, bottom effects and an opposing wind system results in lowering the overall swell energy, while restricted fetch limits evolution of wind seas for the nearshore regions. The study provides a detailed overview on the separate wave systems that influences the local wind-wave climatology of the head Bay of Bengal region. Interesting features such as the diurnal variability and transformation of wave spectra for varying water depths are reported in this study. The study is qualitative in nature due to lack of high-resolution wave spectral data, and the authors believe that this qualitative study is the first information that provides a comprehensive overview on the spectral wave evolution characteristics for the head Bay of Bengal region having wide practical relevance.

A very clear and direct use of this kind of spectral study is recently brought out by Jiang and Mu (2019). The wave spectrum at a location contains information about air-sea interaction at local as well as distant regions. Time series of wave spectra can detect ENSO signature at a location in tropical eastern Pacific Ocean (Portilla et al. 2016; Jiang and Mu 2019). Separate wave system present at a location can be visualized by spectral analysis which cannot be understood from integrated wave parameters even if wind-sea and swell components are partitioned. Different wave systems approaching from different direction with different time period have distinct and specific impact/applications. As aforementioned, high frequency wave system affect navigation and offshore operations and low frequency system find its application in climate studies influencing air-sea exchange. Both direction and frequency of wave systems are must considerable for coastal erosion estimation studies. Large basin-scale seasonal, interannual wind climate modulation can be captured to certain extent by wave spectra at a fixed point (Jiang and Mu 2019). The present analysis could record signature of cyclone Roanu and distant swells reflected from western Australia/Indonesia. It is also believed that wave spectra can track storm activity at a geographically distant region. When considering long-term study of wave spectra, climatic influence of large-scale atmospheric modes like the Southern Oscillation, the Arctic Oscillation, and the Antarctic Oscillation on local wave climate can be brought to light.

5. Summary and Conclusion

The present study made an attempt to explore the spectral evolution of wave characteristics at specific locations over the head Bay of Bengal using a multi-scale nested modeling approach. To accomplish this, the SWAN model was employed to simulate the wave conditions over the study domain using spectral boundary information from WAM for which the computational grid extends up to 70°S to incorporate the Southern Ocean swells. The model simulation was carried out for one complete year of 2016 to have sufficient data to introspect the inter-seasonal variability. To validate the model output, measured data were obtained from a buoy off the Digha coast, and the comparison results in reasonable fidelity. The merged altimeter products and SARAL/AltiKa also showed significant agreement with model's SWH. The monthly averaged wave spectra contain multiple peaks throughout the year emphasizing the coexistence of different wave systems. The predominant features of 1D wave spectra at a deep-water location include two distinct peaks during the post-monsoon, a single peak with higher energy during the southwest monsoon. Considerably high spectral density is also noticed during pre-monsoon season. It attains maximum value during the month of July. Variance density at the buoy location is remarkably lower than the aforementioned location. The time series of 1D spectra at L1 show energy concentration around 0.1–0.15 Hz during the SW monsoon and over two distinct frequency bands, one around 0.1 Hz and another around 0.2 Hz during post-monsoon. During February–April, the wave spectra are centered mainly at 0.12–0.2 Hz. The wave spectral density spreads widely over frequencies for the buoy location compared to the deep-water location. Moreover,

spectral energy exhibits a shift towards the high-frequency side. Transformation of wave spectra along depths at two longitudinal transects has been scrutinized, and significant attenuation of both wind sea and swells are found beyond 100-m water depth towards the coast. During post-monsoon season, reduction of swell energy is associated with wave-bottom interaction and opposing winds, while low wind seas at nearshore result from restricted fetch available for NE winds. Dissipation caused by bottom friction is the primary wave attenuation mechanism for aligned wind seas and swells during the SW monsoon. Higher spectral density, more specifically, higher swell energy, prevails at a series of points over east than locations at the west having similar latitude and almost the same water depths. The directional spectra convey better information on the different wave systems based on information in the spectral space. In addition to S and SSW directions, swells also arrive from the SE due to reflection from western Australia/Indonesia at L1. The direction spread is low during the SW monsoon as both wind seas and swells reach from the SW having almost similar peak frequencies. Variance density associated with wind seas outspreads over directions during November–March. The study also traces wind seas reflected from the coastline. The directional spectra at the buoy location differ from L1 following limited fetch in the north, coastline orientation, bottom friction, and refraction by the bottom. The diurnal variation appears to be significant at the buoy location following coastal breezes. This study thereby develops a preliminary information base of wave spectra over the head Bay of Bengal region. The spectral details can be useful for several applications like climate studies, sediment transport, coastal engineering, navigation, etc. However, there is a need for extensive validation using measurements before operational use. Furthermore, this work can be extended for several years to study the inter-annual variability in the wind-wave system. The identification of wave systems based on occurrence probability of spectral peak position following Portilla et al. (2015) can be undertaken as a separate study with sufficiently long time series of 2D spectra.

Acknowledgements

The authors sincerely thank the Ministry of Human Resources Development (MHRD), Government of India for the financial support. This study is conducted as a part of the Mega Project "Future of Cities" under the module 'Effect of Climate change on local sea level rise and its impact on coastal areas: Kolkata region as a pilot study' supported by MHRD at IIT Kharagpur. The authors are grateful to the Indian National Centre for Ocean Information Services (INCOIS), Ministry of Earth Sciences, Hyderabad, for providing the waverider buoy data.

References

Aboobacker, V. M., Rashmi, R., Vethamony, P., & Menon, H. B. (2011a). On the dominance of pre-existing swells over wind seas along the west coast of India. *Continental Shelf Research, 31,* 1701–1712.

Aboobacker, V. M., Vethamony, P., & Rashmi, R. (2011b). "Shamal" swells in the Arabian Sea and their influence along the west coast of India. *Geophysical Research Letters, 38,* L03608.

Akpınar, A., Bingölbali, B., & Van Vledder, G. P. (2016). Wind and wave characteristics in the Black Sea based on the SWAN wave model forced with the CFSR winds. *Ocean Engineering, 126,* 276–298.

Akpınar, A., van Vledder, G Ph, Kömürcü, Mİ., & Özger, M. (2012). Evaluation of the numerical wave model (SWAN) for wave simulation in the Black Sea. *Continental Shelf Research, 50–51,* 80–99.

Amrutha, M. M., & Sanil Kumar, V. (2017). Observation of dominance of swells over wind seas in the coastal waters of the Gulf of Mannar, India. *Ocean Science, 13,* 703–717.

Baba, M., Dattatri, J., & Abraham, S. (1989). Ocean wave spectra off Cochin, west coast of India. *Indian Journal of Marine Science, 18,* 106–112.

Barstow, S. F., & Kollstad, T. (1991). Field trials of the directional waverider. *Proceedings of the First International Offshore and Polar Engineering Conference, III,* 55–63.

Booji, N., Ris, R. C., & Holthuijsen, L. H. (1999). A third-generation wave model for coastal regions: 1. Model description and validation. *Journal of Geophysical Research, 104*(C4), 7649–7666.

Cavaleri, L., Fox-Kemper, B., & Hemer, M. (2012). Wind-waves in the coupled climate system. *Bulletin of the American Meteorological Society, 93,* 1651–1661.

Cavaleri, L., & Malanotte-Rizzoli, P. (1981). Wind wave prediction in shallow water: theory and applications. *Journal of Geophysical Research, 86*(C11), 10961–10973.

Dee, D. P., Uppala, S. M., Simmons, A. J., Berrisford, P., Poli, P., Kobayashi, S., et al. (2011). The ERA-Interim reanalysis: configuration and performance of the data assimilation system. *Quarterly Journal Royal Meteorological Society, 137*(656), 553–597.

Eldeberky, Y. (1996). *Nonlinear transformation of wave spectra in the nearshore zone (Ph.D. thesis)*. The Netherlands: The Delft University of Technology, Department of Civil Engineering.

Gunther, H., & Behrens, A. (2011). *The WAM model–validation document version 4.5.3. Helmholtz-ZentrumGeesthacht (HZG)*. Teltow: Centre for Materials and Coastal Research.

Hanson, J. L., & Phillips, O. M. (2001). Automated analysis of ocean surface directional wave spectra. *The Journal of Atmospheric and Oceanic Technology, 18,* 277–293.

Hasselmann, K., Barnett, T. P., Bouws, E., Carlson, H., Cartwright, D. E., Enke, K., et al. (1973). *Measurements of wind-wave growth and swell decay during the Joint North Sea Wave Project (JONSWAP). Ergnzungsheft zur Deutschen Hydrographischen Zeitschrift Reihe* (p. 95). Hamburg: Deutsches Hydrographisches Institute.

Holthuijsen, L. H., Booij, N., & Ris, R. C. (1993). A spectral wave model for the coastal zone. In *Proceedings 2nd international symposiumon ocean wave measurement and analysis*, New Orleans, Louisiana, July 25–28, 1993, NewYork, pp. 630–641.

Janssen, P. A. E. M. (1989). Wave induced stress and the drag of air flow over sea water. *Journal of Physical Oceanography, 19,* 745–754.

Janssen, P. A. E. M. (1991). Quasi-linear theory of wind-wave generation applied to wave forecasting. *Journal of Physical Oceanography, 21,* 1631–1642.

Jiang, H., & Mu, L. (2019). Wave climate from spectra and its connections with local and remote wind climate. *Journal of Physical Oceanography*, *49*, 543–559.

Kumar, V. S., Anand, N. M., Kumar, K. A., & Mandal, S. (2003). Multi-peakedness and groupiness of shallow water waves along Indian coast. *The Journal of Coastal Research, 19,* 1052–1065.

Kumar, V. S., Dubhashi, K. K., & Nair, T. M. B. (2014). Spectral wave characteristics off Gangavaram, Bay of Bengal. *Journal of Oceanography, 70,* 307–321.

Longuet-Higgins, M. S. (1969). A nonlinear mechanism for the generation of sea waves. *Proceedings of the Royal Society A: Mathematical, Physical and Engineering Science, 311*(1506), 371–389.

Mazaheri, S., Kamranzad, B., & Hajivalie, F. (2013). Modification of 32 years ECMWF wind field using QuikSCAT data for wave hindcasting in Iranian Seas. *Journal of Coastal Research: Speciaal Issue, 65,* 344–349.

McComb, P., Johnson, D., & Beamsley, B. (2009). Numerical model study to reduce swell and long wave penetration to Port Geraldton. In *Proceedings of the 2009 pacific coasts and ports conference*, *Coasts and ports 2009: In a dynamic environment,* Wellington, September 16–18, 2009, pp. 490–496.

Moeini, M. H., Etemad-Shahidi, A., Chegini, V., & Rahmani, I. (2012). Wave data assimilation using a hybrid approach in the Persian Gulf. *Ocean Dynamics, 62,* 785–797.

Nayak, S., Bhaskaran, P. K., Venkatesan, R., & Dasgupta, S. (2013). Modulation of local wind–waves at Kalpakkam from remote forcing effects of Southern Ocean swells. *Ocean Engineering, 64,* 23–35.

Parvathy, K. G., Umesh, P. A., & Bhaskaran, P. K. (2017). Interseasonal variability of wind–waves and their attenuation characteristics by mangroves in a reversing wind system. *The International Journal of Climatology*. https://doi.org/10.1002/joc.5147.

Patra, A., & Bhaskaran, P. K. (2016). Trends in wind–wave climate over the head Bay of Bengal region. *The International Journal of Climatology, 36,* 4222–4240.

Patra, A., & Bhaskaran, P. K. (2017). Temporal variability in wind–wave climate and its validation with ESSO-NIOT wave atlas for the head Bay of Bengal. *Climate Dynamics, 49,* 1271–1288.

Portilla, J., Cavaleri, L., & Van Vledder, G. (2015). Wave spectra partitioning and long term statistical distribution. *Ocean Modelling, 96,* 148–160.

Portilla, J., Salazar, A., & Cavaleri, L. (2016). Climate patterns derived from ocean wave spectra. *Geophysical Research Letters*, *43*, 11736–11743.

Ris, R. C., Holthuijsen, L. H., & Booij, N. (1999). A third-generation wave model for coastal regions: 2 verification. *Journal of Geophysical Research, 104*(C4), 7667–7681.

Rosmorduc, V., Benveniste, J., Bronner, E., Dinardo, S., Lauret, O., Maheu, C., Milagro, M., & Picot, N. (2011). In J. Benveniste and N. Picot (Eds.), *Radar altimetry tutorial*. http://www.altimetry.info. Accessed 20 Mar 2018.

Sabique, L., Annapurnaiah, K., Balakrishnan Nair, T. M., & Srinivas, K. (2012). Contribution of southern Indian Ocean swells on the wave heights in the northern Indian Ocean—a modeling study. *Ocean Engineering, 43,* 113–120.

Saket, A., Etemad-Shahidi, A., & Moeini, M. H. (2013). Evaluation of ECMWF wind data for wave hindcast in Chabahar zone. *The Journal of Coastal Research Special Issue, 65,* 380–385.

Samiksha, S. V., Polnikov, V. G., Vethamony, P., Rashmi, R., Pogarskii, F., & Sudheesh, K. (2015). Verification of model wave heights with long-term moored buoy data: application to wave field over the Indian Ocean. *Ocean Engineering, 104,* 469–479.

Sandhya, K. G., Balakrishnan Nair, T. M., Bhaskaran, P. K., Sabique, L., Arun, N., & Jeykumar, K. (2014). Wave forecasting system for operational use and its validation at coastal Puducherry, east coast of India. *Ocean Engineering, 80,* 64–72.

Sandhya, K. G., Remya, P. G., Balakrishnan Nair, T. M., & Arun, N. (2016). On the co-existence of high-energy low-frequency waves and locally- generated cyclone waves off the Indian east coast. *Ocean Engineering, 111,* 148–154.

Shanas, P. R., Aboobacker, V. M., Albarakati, A. M. A., & Zubier, K. M. (2017). Superimposed wind-waves in the Red Sea. *Ocean Engineering, 138,* 9–22.

Soares, C. G. (1991). On the occurrence of double peaked wave spectra. *Ocean Engineering, 18*(1/2), 167–171.

Stopa, J. E., & Cheung, K. F. (2014). Intercomparison of wind and wave data from the ECMWF Reanalysis Interim and the NCEP Climate Forecast System Reanalysis. *Ocean Modelling, 75,* 65–83.

Stopa, J. E., Cheung, K. F., & Chen, Y. L. (2011). Assessment of wave energy resources in Hawaii. *Renewable Energy, 36*(2), 554–567.

SWAN Team (2012). SWAN user manual. SWAN Cycle III version 40.85. Delft University of Technology, Technical

Documentation, Delft, Netherlands, pp 94. http://www.swan.tudelft.nl. Accessed 22 Mar 2018.

Tolman, H. L. (1991). A third generation model for wind waves on slowly varying, unsteady and inhomogeneous depths and currents. *Journal of Physical Oceanography*, *21*, 782–797.

Umesh, P. A., Bhaskaran, P. K., Sandhya, K. G., & Balakrishnan Nair, T. M. (2017). An assessment on the impact of wind forcing on simulation and validation of wave spectra at coastal Puducherry, east coast of India. *Ocean Engineering, 139,* 14–32.

Umesh, P. A., Bhaskaran, P. K., Sandhya, K. G., & Balakrishnan Nair, T. M. (2018). High frequency tail characteristics in the coastal waters off Gopalpur, Northwest Bay of Bengal: a nearshore modeling study. *Pure and Applied Geophysics, 175,* 2351–2379.

WAMDIG. (1988). The WAM model —a third generation ocean wave prediction model. *Journal of Physical Oceanography, 18,* 1775–1810.

Wandres, M., Pattiaratchi, C., Hetzel, Y., & Wijeratne, E. M. S. (2017). The response of the southwest Western Australian wave climate to Indian Ocean climate variability. *Climate Dynamics*. https://doi.org/10.1007/s00382-017-3704-z.

Wang, X. L., & Swail, V. R. (2002). Trends of Atlantic wave extremes as simulated in a 40-yr wave hindcast using kinematically reanalyzed wind fields. *Journal of Climate, 15*(9), 1020–1035.

Zijlema, M., & van der Westhuysen, A. J. (2005). On convergence behaviour and numerical accuracy in stationary SWAN simulations of nearshore wind wave spectra. *Coastal Engineering, 52,* 237–256.

(Received August 24, 2018, revised July 26, 2019, accepted July 29, 2019, Published online August 7, 2019)